FUDMA Journal of Sciences (FJS)
ISSN online: 2616-1370
ISSN print: 2645 - 2944
Vol. 10 No. 18, September, 2026, pp 58 – 70
DOI: https://doi.org/10.33003/fjs-2026-1018-5688

Application of Dubinin-Radushkevich Isotherms and Density Functional Theory to Phenolic Contaminant Remediation Using Mg-Activated Snail Shell Biochar

***[1,2]Hitler Louis, [2]Theresa O. Egbuchunam and [2]Idongesit J. Mbonu**

[1]Department of Chemistry, Federal University of Petroleum Resources, Effurun, Delta State, Nigeria.
[2]Department of Pure and Industrial Chemistry, University of Calabar, Calabar, Cross River, Nigeria.

*Corresponding authors' email: louis.hitler@unical.edu.ng

Received: 05 Aug. 2026
Accepted: 15 Aug. 2026
Published: 18 Sep. 2026

ABSTRACT
This study applies the Dubinin-Radushkevich-Misra (DRM) isotherm and density functional theory (DFT) to investigate the adsorption and molecular interactions of phenol (PNL) and para-chlorophenol (PCP) on Mg-modified snail shell biochar (Mg@SSB). The Langmuir model provided good fits, with values of 0.9860-0.9970 for PNL and 0.9834-0.9921 for PCP, and maximum adsorption capacities (q_{max}) of 11.16-11.85 and 12.64-13.30 mg/g, respectively. The DRM model showed stronger correlations (R^2), with predicted maximum adsorption amounts of 14.84 mg/g for PNL and 57.81 mg g for PCP. The corresponding DRM adsorption energies (E_{ads}) were 9.42 and 13.61 kJ mol, respectively, indicating stronger adsorption of PCP. Kinetic analysis showed that the Weber-Morris intraparticle diffusion model provided the highest correlations for both PNL and PCP, exceeding those obtained from the pseudo-first-order, pseudo-second-order, and Elovich models. DFT calculations further supported preferential PCP adsorption, with adsorption energies of -1.1683 eV for PCP–Mg@SSB and -0.8163 eV for PNL–Mg@SSB. For the pristine Mg@SSB surface, the calculated HOMO, LUMO, and HOMO–LUMO gap were -4.978, -2.997, and 1.981 eV, respectively. The consistently stronger DRM and DFT adsorption characteristics of PCP demonstrate its greater affinity for Mg@SSB, while the high DRM correlations provide additional mechanistic information beyond the Langmuir model. These findings show Mg@SSB's potential for remediating phenolic contaminants and highlight the complementary value of DRM modelling and DFT in elucidating adsorption behaviour.

Keywords: *MgO-biochar; phenol; p-chlorophenol; adsorption; isotherm; kinetics; DFT*

INTRODUCTION

Phenol and its derivatives are frequently released into the environment through several industrial processes, including pharmaceutical, petroleum, petrochemical, pesticide, plastics, and paper manufacturing (Panigrahy *et al*., 2022; Ahmaruzzaman, *et al*., 2024). Consequently, these compounds are recognized as persistent environmental contaminants. Global phenol production was estimated to have reached approximately 7.8 million tons in 2001 (Kujawski *et al*., 2004). Specific phenolic compounds, like para-chlorophenol (PCP), are especially hazardous since they add an objectionable taste and smell to drinking water and are also toxic to aquatic life and humans (Mhlongo, 2021). Even at very low levels, their presence can pose a barrier to public acceptance of recycled water. Therefore, the U.S. Environmental Protection Agency (EPA) classified phenolic compounds as priority pollutants because of their toxicity, persistence, and ubiquity (Wang *et al*., 2021).

Biochar is a carbon-rich material containing aromatic structures and mineral phases, produced through the pyrolysis of biomass under controlled conditions. The European Biochar Certificate (EBC) defines biochar based on its production from sustainably sourced biomass through controlled thermal conversion (Schmidt *et al*., 2016). Both feedstock characteristics and pyrolysis temperature influence the physicochemical properties of biochar and, consequently, its interaction with contaminants (Hassan *et al*., 2020). In particular, pyrolysis temperature governs the development of surface area, pore structure, and microporosity, thereby affecting the distribution and retention of contaminants on the carbonized material (Tomczyk *et al*., 2020). These properties, together with its relative stability against rapid mineralization, have made biochar an attractive adsorbent for the removal of persistent pollutants from wastewater (Gómez-Pastora *et al*., 2014). Furthermore, the surface properties and porosity of biochar can be greatly enhanced when metals such as magnesium (Mg) are added, creating active sites that increase pollutant interactions and thereby improve the efficiency of biochar adsorption of phenolic compounds in contaminated water (Qiu *et al*., 2020).

Among the available approaches for phenolic contaminant removal, adsorption remains attractive because of its operational simplicity, cost-effectiveness, and adaptability to different wastewater matrices. Kumar *et al.* 2021, for example, engineered biochar from wood apple shell waste for the removal of phenol, 4-chlorophenol (4-CPh), and 2,4-dichlorophenol (2,4-DCPh), obtaining maximum uptake capacities of 102.71, 172.24, and 226.55 mg/g, respectively, at 30 ± 1 °C. These results demonstrated the potential of biomass-derived biochar for phenolic contaminant removal. Similarly, Fseha *et al.* 2023 investigated date palm frond biochar for phenol adsorption from effluent and reported an optimum pH of 6, a contact time of 20 h, and an adsorbent dosage of 0.1 g, corresponding to a maximum adsorption capacity of 15.93 mg/g. Phenol removal efficiencies of 60% and 85% were reported for primary- and secondary-treated wastewater, respectively. Dong *et al.* 2021 developed a biochar-based iron oxide composite (FeYBC) for simultaneous Cr(VI) and phenol removal from water. The adsorption of the two contaminants exhibited different thermal characteristics, with maximum adsorption amounts of 24.37 mg/g for Cr(VI) and 39.32 mg/g for phenol. Snail-

shell-derived biochar represents a particularly interesting precursor because of the abundance of snail-shell waste, its high calcium content (>99%), and the mineral-rich structure that can provide an inorganic component alongside the carbonaceous fraction (Nhung *et al*., 2023). The potential of snail-shell-derived materials for environmental applications has been demonstrated in previous studies. Vu *et al*. 2024 investigated Golden Snail Shells (*Pomacea canaliculata* L.) produced through pyrolysis for phosphorus adsorption from aqueous solution. Alumonah *et al*. 2024 investigated *Achatina fulica* snail shells for the removal of heavy metals from produced water associated with the oil and gas industry. Similarly, An *et al*. 2022 combined chestnut-shell activated carbon with pyrolyzed snail shells for methylene blue adsorption from wastewater. These studies demonstrate the potential of snail-shell-derived materials as low-cost precursors for wastewater treatment; however, the adsorption behavior of Mg-modified snail-shell biochar toward phenolic contaminants and the molecular basis of its selectivity toward phenol and PCP remain insufficiently understood.

In this study, Mg modification was therefore employed to alter the physicochemical properties of experimentally characterized snail-shell biochar and to investigate its effect on the adsorption of phenol (PNL) and PCP. The material was characterized using FT-IR, BET surface analysis, X-ray diffraction (XRD), and scanning electron microscopy coupled with energy-dispersive X-ray spectroscopy (SEM-EDX), followed by batch adsorption experiments while DFT calculations complemented the experimental results by providing molecular-level information. In addition to conventional adsorption analysis, the Dubinin-Radushkevich-Misra (DRM) isotherm was specifically employed to obtain information on the adsorption capacity and characteristic adsorption energy of the system. Unlike empirical three-parameter models such as the Sips and Redlich-Peterson equations, which primarily improve the mathematical description of heterogeneous adsorption equilibria, the DRM approach provides an energetic parameter that can be used to interpret the nature and strength of adsorbate-adsorbent interactions. This distinction is particularly relevant for Mg-modified snail-shell biochar because its adsorption surface is expected to contain both heterogeneous carbonaceous domains and mineral/Mg-containing sites.

MATERIALS AND METHODS

Preparation, Modification, and Characterization

The pyrolysis method was adopted for the preparation of the biochar from snail shell materials as described in earlier studies (Saghir *et al*., 2022). The prepared snail shell materials were converted to micro-sized powdered material and then pyrolyzed at a temperature of 700 ^{o}C for an hour in a muffle furnace with an oxygen-limited atmosphere to obtain pristine snail shell biochar (SSB). To prepare the activated material, 20 g of the snail shell biochar (SSB) was immersed in 40 mL of a 0.5 M solution of activating agent ($MgSO_4$) and was dried in an oven at 100 °C for 24 hours. The resulting materials were then pulverized, sieved through a 200-mesh sieve, and stored for the adsorption experiment. The synthesized Mg-modified snail shell biochar (Mg@SSB) material was experimentally characterized using FT-IR, X-ray diffraction (XRD) analysis, BET surface analysis, and Scanning Electron Microscopy with Energy Dispersive X-ray Spectroscopy (SEM-EDX) as shown in Scheme 1.

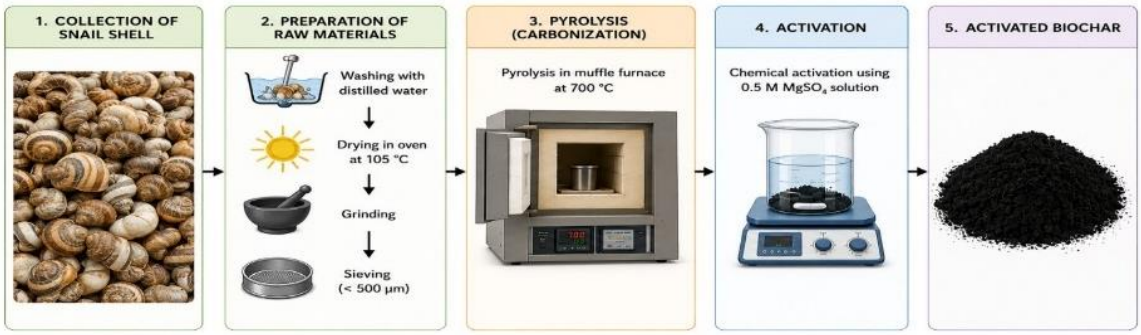

Scheme 1: Experimental procedure for the preparation and activation of the MgO-doped biochar

Batch Adsorption Tests

The isotherm studies were carried out with p-chlorophenol (PCP) and phenol (PNL) solutions using an adsorbent dosage of 1.0 gram, a solution pH of 6.0, an adsorption contact time of 180 minutes, and at varying initial concentrations of 5, 10, 20, 40, 60, 120, 150, 200, 250, and 300 mg/L at temperatures of 25, 35, and 45 °C. For each of the experiments, the suspension was filtered using Whatman filter paper, and the remaining adsorbate concentration in the liquid after filtration was determined using a UV-VIS spectrometer at wavelengths of 280 and 270 nm for para-chlorophenol and phenol, respectively (Hamdaoui and Naffrechoux 2007). Adsorption capacity over time (Q_t) and equilibrium adsorption capacity (Q_e) were resolved, corresponding to equations (1) and (2)

$$Q_t(\mathrm{mg/g}) = \frac{(C_0 - C_t)V}{m} \quad (1)$$

$$Q_e(\mathrm{mg/g}) = \frac{(C_0 - C_e)V}{m} \quad (2)$$

The evaluated adsorption capacity Q_e and the equilibrium concentrations C_e were utilized for modelling the various adsorption isotherms selected for this investigation. In this research work, nine (9) adsorption isotherms: Langmuir, Freundlich, Sips, Temkin-I, Temkin-II, Redlich-Peterson (R-P), Dubinin-Radushkevich (DR), Dubinin-Astakhov (DA), and Dubinin-Radushkevich-Misra (DRM) were fitted to the experimental data as expressed in Table 1 (Guo *et al*., 2025; Chu *et al*., 2022; Chu, 2021; Chu *et al*., 2024a; Chu *et al*., 2024b)

Table 1: Isotherm Models Utilized in this Study

Isotherm Models	Equations
Langmuir	$q_e = q_m \frac{K_L C_e}{1+K_L C_e}$
Freundlich Isotherm	$q_e = K_F C_e^{1/n}$
Sips isotherm	$q_e = \frac{q_m K_s C_e^n}{1+K_s C_e^n}$
Temkin-I Isotherm	$q_e = q_T ln(K_T C_e)$
Temkin-II Isotherm	$q_e = q_T ln(1 + K_T C_e)$
Redlich-Peterson (R-P)	$q_e = \frac{aC_e}{1+bC_e^n}$
DR	$q_e = q_m exp\left\{-\left[\beta ln\left(\frac{C_s}{C_e}\right)\right]^2\right\}$
DA	$q_e = q_m exp\left\{-\left[\beta ln\left(\frac{C_s}{C_e}\right)\right]^n\right\}$
DRM	$q_e = q_m exp\left\{-\left[\beta ln\left(1+\frac{\alpha}{C_e}\right)\right]^2\right\}$

In the Langmuir Isotherm q_m and K_L is the maximum adsorption capacity (mg/g) and the Langmuir equilibrium constant (L/mg), respectively. In the Freundlich Isotherm and represent the distribution coefficient and the adjustable parameter, respectively. The K_F quantity is measured in $(mg/g)(L/mg)^{-1/n}$. For the Sips isotherm, the equilibrium parameters ,q_m, K_s and n are the maximum adsorption capacity, the equilibrium constant, and the fitting parameter, respectively. According to the Temkin-I Isotherm, $q_T = q_m RT/b_T$ which is the surface capacity for pollutant adsorption per unit binding energy, measured in mg/g, while the b_T is the heat of adsorption (J/mol). In the Redlich-Peterson Isotherm, the q_e (mg/g) quantity corresponds to the solid phase concentration of the adsorbent. The a, b , and n are the adjustable fitting parameters. For the Dubinin-Radushkevich isotherm derivatives, β is a dimensionless parameter, which is expressed as RT/E_a , where E_a quantity signifies the adsorption energy and q_m is the maximum adsorption capacity (mg/g), α is an adjustable parameter. Furthermore, C_s is the solubility of the adsorbates according to earlier studies on the adsorption and modeling of chlorophenols using the Dubinin-Radushkevich isotherm (Mahanty et al., 2023).

The adsorption kinetics of phenol (PNL) and para-chlorophenol (PCP) onto the magnesium-modified biochar (MgSO4-SSB) were systematically evaluated using the Pseudo-First-Order (PFO), Pseudo-Second-Order (PSO), and Elovich kinetic models to elucidate rate-controlling mechanisms and surface reactivity differences among materials, as presented in equations (3) – (5).

Pseudo-first order (PFO):

$$q_t = q_e\left[1 - \exp\left(-k_1 t\right)\right] \quad (3)$$

Pseudo-second order (PSO): $q_t = \frac{q_e^2 k_2 t}{1+q_e k_2 t}$ (4)

The Elovich kinetics: $\frac{dq_t}{dt} = \alpha e^{-\beta q_t}$ (5)

Where q_t (mg/g), k_1 (min−1), and k_2 (g mg−1 min−1) are the adsorption capacity of H_2SO_4@SSB, the rate constant for the PFO, and the PSO kinetics, respectively, while the α (mg/(g min)) and β (g/mg) parameters embedded in the Elovich kinetics signify the adsorption rate and the extent of surface coverage, respectively (Lima et al., 2021). To model the Pseudo-First-Order (PFO), Pseudo-Second-Order (PSO), Elovich, and the Weber–Morris intraparticle diffusion (IPD) kinetics, experiments were conducted to evaluate the effect of contact time at intervals of 10, 30, 60, 90, 120, and 150 minutes. These experiments were optimized at a pH of 6.0, a dosage of 1.0 gram, a temperature of 25 °C, and an initial concentration of 50 mg/L of PNL/PCP in a 50 mL conical flask

Theoretical Methodology

To investigate the electronic structure, adsorption behavior, and charge transfer interactions between the Mg@SSB and its adsorption complexes with phenol (PNL) and p-chlorophenol (PCP), the Density Functional Theory (DFT) calculations were performed in gas phase without an explicit or implicit solvent model (Ji *et al*., 2024; Yu *et al*., 2024). The Gaussian09 software package was used for all quantum chemical calculations, while molecular structures were constructed and displayed with the use of the GaussView 6.0.16 software package (Frisch *et al*., 2016; Dennington *et al*., 2016). The geometry optimizations for the model of the adsorbent and the complexes of the adsorbent–adsorbate were carried out using the hybrid exchange-correlation functional Becke three-parameter Lee-Yang-Parr (B3LYP) with the long-range van der Waals dispersion correction (D3) along with the Def2-SVP basis set (Grimme *et al*., 2010; Weigend & Ahlrichs, 2005).

RESULTS AND DISCUSSION

Biochar Characterization

Surface Analysis and Morphology

The surface elemental composition of Mg-SSB was investigated by energy-dispersive X-ray spectroscopy (EDX), and the corresponding spectrum is presented in Figure 1. The analysis detected Ca, S, Mg, Al, Sn, Si, and K on the Mg-SSB surface. Calcium was the predominant detected element, accounting for 60.01 wt%, consistent with the calcium-rich mineral composition expected for snail-shell-derived material. Magnesium accounted for 13.01 wt%, confirming the presence of Mg on the modified biochar surface. Sulfur was also detected at 21.48 wt%, indicating the retention of sulfur-containing species following the $MgSO_4$ treatment. Minor amounts of Al (3.40 wt%), Sn (1.43 wt%), Si (0.42 wt%), and K (0.25 wt%) were also detected. The EDX results confirm the elemental incorporation and surface heterogeneity of the modified material; however, EDX alone does not establish the chemical phases or oxidation states of the detected elements. Therefore, the assignment of specific Mg-, Ca-, or S-containing phases was based on the complementary XRD and FTIR characterization rather than on EDX elemental composition alone. Notably, carbon and oxygen were not included among the quantitatively reported elements in the EDX dataset; consequently, their concentrations were not inferred from the present analysis. The elemental profile nevertheless demonstrates the mineral-rich nature of Mg-SSB and confirms the successful presence of Mg following modification (Yin *et al*., 2025). This,

combined with the microstructural roughness observed, suggests that Mg modification provides increased chemical heterogeneity and surface characteristics.

Table 2: EDX Elemental composition of Mg-SSB material

Element Number	Element Symbol	Element Name	Atomic Conc.	Weight Conc.
20	Ca	Calcium	52.32	60.01
16	S	Sulfur	23.40	21.48
12	Mg	Magnesium	18.70	13.01
13	Al	Aluminium	4.40	3.40
50	Sn	Tin	0.42	1.43
14	Si	Silicon	0.53	0.42
19	K	Potassium	0.22	0.25

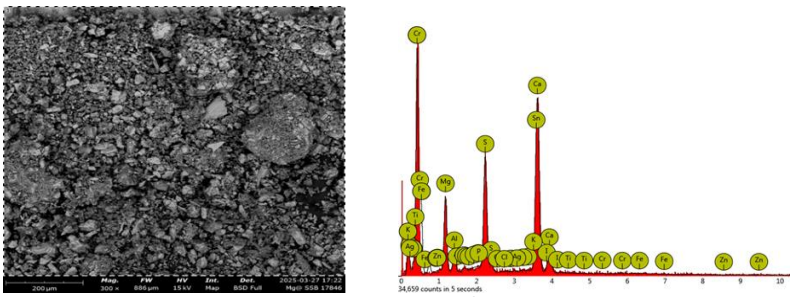

Figure 1: SEM micrograph and EDX spectrum of Mg-SSB material

BET Surface Analysis

The values of the BET, Barrett-Joyner-Halenda (BJH), Dollimore-Heal (DH), Dubinin-Radushkevich (DR), and Dubinin-Astakhov (DA) methods are given in Table 3. The parameters give important information about the surface properties, pore structure, and adsorption capacity of the biochar material that has been synthesized (Rai *et al*., 2025). The BET surface area analysis showed a significant increase in the specific surface area after the magnesium modification. The estimated surface area of SSB increased substantially following Mg modification. The Langmuir-derived surface area increased from 88.79 m^2/g for pristine SSB to 822.85 m^2/g for Mg@SSB. Consistent increases were also observed in the surface-area estimates obtained using the BJH, DH, and DR methods, which increased from 51.96 m^2/g for SSB to 167.90, 178.70, and 159.60 m^2/g for Mg@SSB, respectively. The pronounced increase in these surface-area estimates suggests that Mg treatment altered the pore structure of SSB, potentially through the opening of previously inaccessible pores and the development of additional porous features.

The pore volume analysis also shows that the porous structure of the biochar is improved with the incorporation of magnesium. The BJH pore volume (SBB) increased from 0.023 cc/g to 0.083 cc/g for Mg-SSB, and the DH pore volume (SBB) increased from 0.024 cc/g to 0.085 cc/g for Mg-SSB. Likewise, the DR pore volume jumped sharply from 0.002 cc/g to 0.057 cc/g, which is almost a 28-fold increase. The increased pore volumes suggest that magnesium modification created a more developed pore network that could accommodate more molecules of adsorbate (Yin *et al*., 2025). In addition, the pore size distribution was found to have some changes following the modification. The BJH and DH methods indicate that the average diameter of pores increased from 1.453 nm (SSB) to 2.137 nm (Mg-SSB). Similarly, the DR pore size was also changed from 2.965 nm to 6.195 nm, and the DA pore diameter was increased from 1.820 nm to 2.920 nm.

Table 3: Surface Area, Pore Volume, and Pore Size of the Pristine and Modified Biochar

Biochar Materials	Surface Area (m^2/g)			
	Langmuir BET	BJH	DH	DR
SSB	88.79	51.96	56.92	82.69
Mg-SSB	822.85	167.9	178.7	159.6
	Pore Volume (cc/g)			
	BJH	DH	DR	
SSB	0.023	0.024	0.002	
Mg-SSB	0.083	0.085	0.057	
	Pore Size (nm)			
	BJH	DH	DR	DA
SSB	1.453	1.453	2.965	1.820
Mg-SSB	2.137	2.137	6.195	2.920

Powdered X-Ray Diffraction (XRD) Analysis

The results of powdered X-ray diffraction (XRD) analysis of the mineral composition and phase percentage of the $MgSO_4$-based modified biochar (Mg-SSB) materials are shown in Table 4 and Figure 2, respectively. A typical X-ray diffraction (XRD) display of the Mg-modified sample (Mg-SSB) is shown in Figure 2. A crystallographic assembly consisting of a primary phase of calcite ($CaCO_3$), a secondary phase of

periclase (MgO), and another secondary phase of quartz (SiO_2) is clearly seen in the diffraction peaks. The quantitative phase analysis reveals that the crystalline fraction is made of about 74.0 % CaCO3, 16.0 % MgO, and 10.0 % SiO_2 (Table 3). The fact that calcite is still the major phase suggests that the carbonate matrix has not been structurally altered after adding Mg. In the meantime, the well separated peaks of MgO indicate that the periclase has crystallized as a distinct crystalline phase and not been incorporated into the calcite lattice (Rai *et al*., 2025; Karami *et al*., 2020). These results were also corroborated by the SEM-EDX results, which showed that the sample contained high quantities of Ca (52.32 wt.%), S (23.40 wt.%), and Mg (18.70 wt.%). The strong CaCO3 peaks are related to the high Ca content, whereas the Mg signal is attributable to the crystalline MgO, which was detected by XRD. The relatively high sulfur content found in EDX, though, is not matched by any specific sulfate peaks in the XRD pattern. The quartz fraction (10 %) does not change chemically under the modification conditions, and this is why it is found as a minor crystalline phase. Based on the angular morphology observed in SEM, it is suggested that it is a resistant siliceous component. Chemically, the presence of basic MgO and CaCO3 within the Mg-SSB matrix suggests that there is considerable surface chemistry change.

Table 4: Relative Abundance of Mineral Phases (%) of the Mg-chemically Modified Biochar Material

Mineral Composition	Chemical Formula	Abundance (%)
Quartz	SiO_2	10.0
Periclase	MgO	16.0
Calcite	$CaCO_3$	74.0

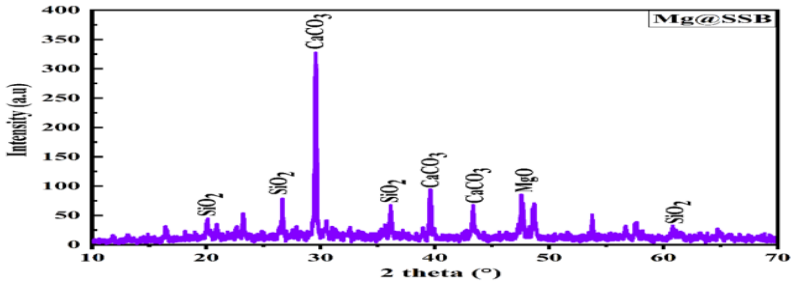

Figure 2: Powdered XRD spectral analysis of Mg-SSB material

Surface Chemistry using FT-IR Analysis

To investigate the surface functional groups present on both biochar and to assess the modifications in the chemical properties resulting from the processing of the biochar with magnesium, FT-IR analysis was used (Mustapha *et al*., 2026). Figure 3 shows that both materials contain oxygen-related functional groups and that Mg impregnation brought about significant changes in the peak intensity and position, suggesting that surface modification was achieved. The presence of a broad absorption band in both samples around 3200-3600 cm^{-1} is due to the stretching mode of hydroxyl (-OH) groups from adsorbed water molecules and/or phenolics/alcoholic functionalities. This band is slightly lower in intensity for the Mg@SSB, indicating that the impregnation process involved interaction of Mg ions with hydroxyl groups so that some hydroxyl groups were consumed or coordinated to the Mg ions. The band of medium intensity at 2920–2850 cm^{-1} is attributed to the asymmetric and symmetric stretching of aliphatic C–H bonds from the cellulose and lignin residues.

Two strong bands of absorption are found around 1600-1450 cm^{-1}, which are attributed to stretching of the C = C bonds of aromatic compounds and asymmetric stretching of the carboxylate (COO-) groups. This band gets weaker upon magnesium modification, indicating interaction of oxygen-containing functional groups like carboxyl and phenolic with Mg^{2+} ions. These interactions are representative of the chemical bonding between the magnesium species and the surface of the biochar. The absorption region (1200-1000cm^{-1}) is mostly due to the C–O (alcohols) and C–O–C (ethers) stretching vibrations and C–OH (phenols) stretching vibrations (Yu *et al*., 2021). This region is wider in the Mg@SSB spectrum and shows some shifts relative to pure SSB, consistent with the chemical environment of these oxygen-containing groups having been changed by the magnesium impregnation. The most pronounced difference between the two spectra is in the 800–500 cm^{-1} region. The absorption bands within this range are stronger in the case of the Mg@SSB sample, which are believed to be due to the formation of Mg–O stretching vibrations and thus the successful incorporation of magnesium oxide or magnesium hydroxide species onto the biochar surface. Because no such functional groups are present or less pronounced in pure SSB, the modification process was successful, as evidenced. All the observed changes in hydroxyl, carboxyl, and C–O vibrations, along with the appearance of Mg–O vibrations, are a testament to the successful synthesis of Mg@SSB.

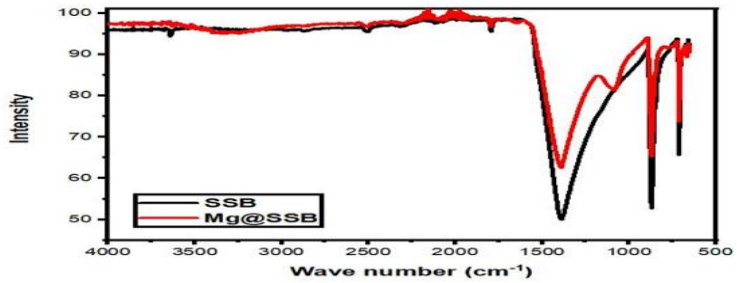

Figure 3: FT-IR spectrum showing frequencies of pristine SSB and Mg@SSB

Isotherm Modeling

Langmuir, Freundlich, Sips, Temkin-I, and Redlich–Peterson Isotherm Models

The adsorption equilibrium of phenol (PNL) and para-chlorophenol (PCP) was investigated with Mg-modification of the biochar prepared from snail shells at 25°C, 35°C, and 45°C using the Langmuir, Freundlich, Sips, Temkin-I, and Redlich–Peterson isotherm representations. The maximum adsorption capacity (q_{max}), correlation coefficient (R^2), and other parameters directly indicate the adsorption productivity and the reliability of the adsorption models, as shown in Table 5 (a) and (b), while the graphical fit of the adsorption equilibrium at every adsorption temperature is shown in Figures 4 and 5.

The obtained R^2 values for both PNL (0.9860-0.9970) and PCP (0.9834-0.9921) were high for the Langmuir isotherm, which yielded reasonably good conformity with the monolayer adsorption assumptions of Mikolajczyk *et al*. 2026, and are shown in Table 4 (a) and (b) for PNL and PCP, respectively (Mikolajczyk *et al*., 2026). The Langmuir maximum adsorption capacity was found to be least sensitive to temperature changes for PNL, rising marginally from 11.54 mg g^{-1} at 25 °C to 11.85 mg g^{-1} at 35 °C and then declining to some extent to 11.16 mg g-1 at 45 °C. This behavior indicates that there are limited thermal activation sites available for the monolayer and early saturation of the available adsorption sites. The same tendency was observed for PCP with q_{max} of 13.13 – 13.30 mg g^{-1} at 25 - 35 °C and a decrease to 12.64 mg g^{-1} at 45 °C, indicating that the monolayer affinity of PCP is slightly higher than that of PNL on Mg-SSB. The Freundlich model is a model of adsorption on heterogeneous surfaces, especially at high temperatures (Yang, 1998). Good multilayer adsorption behaviour was observed with the values of the correlation coefficients, which ranged from 0.9898 to 0.9940 for PNL and 0.9948 to 0.9972 for PCP. In all the cases, the Freundlich intensity parameter was found to be greater than unity, which indicates favourable adsorption conditions. In the case of PNL, the n value rose from 1.84 to 2.11 with an increase in temperature from 25 °C to 45 °C, and in the case of PCP, the n value rose from 1.75 to 2.03 with the increase in temperature from 25 °C to 45 °C. The trends indicate better adsorption as the temperature is increased, particularly for PCP.

The Sips isotherm was always the best-fitting isotherm for all the models, as it combined the characteristics of both Langmuir and the Freundlich isotherms to describe the surface heterogeneity and saturation effect simultaneously. The R^2 values were high, from 0.9960 to 0.9985 for PNL and 0.9967 to 0.9984 for PCP, throughout all the temperatures. The Sips maximum adsorption capacity displayed a substantial rise with the rise in temperature for PNL from 14.14 mg g^{-1} at 25 °C to 21.05 mg g-1 at 45 °C, indicating high thermal activation and good adsorption site accessibility. The Redlich–Peterson model exhibited the best statistical agreement, with R^2 values greater than 0.9967 for PNL and 0.9976 for PCP. With Mg-SSB, the adsorption capacity of PCP is always much higher than that of PNL, especially in the Redlich-Peterson model. The effect of temperature on the adsorption capacity of PCP with an increasing amount of both adsorbates further indicates an endothermic adsorption process, which is controlled by heterogeneous surface interactions, at 45 °C. In general, the isotherm patterns for the adsorption of both PNL and PCP on Mg-SSB were in the following order of performance: Redlich–Peterson>Sips> Langmuir >Temkin-I.

Table 5 (a): Isotherm parameters for PNL adsorption onto Mg-SSB

Isotherm Models	Parameters	Units	25 ºC	35 ºC	45 ºC
Langmuir					
	q_{max}	(mg/g)	11.54	11.845	11.1639
	K_L	(L/mg)	0.0173	0.0192	0.02916
	R^2	-	0.9970	0.9930	0.9860
Freundlich					
	K_F	$(mg/g)(L/mg)^{-1/n}$	0.5953	0.6549	0.95885
	n	-	1.8412	1.8578	2.10799
	R^2	-	0.9898	0.9901	0.9940
Sips					
	q_{max}	(mg/g)	14.139	16.412	21.0483
	K_S	(L/g)	0.0212	0.0237	0.03531
	n	-	0.8512	0.7906	0.6388
	R^2	-	0.9985	0.9960	0.9976
Temkin-I					

Isotherm Models	Parameters	Units	25 ºC	35 ºC	45 ºC
	q_T	(J/mol)	1.8042	1.8453	1.6868
	K_T	(L/g)	0.4248	0.4815	0.9211
	R^2	-	0.9246	0.9228	0.9261
Redlich-Peterson					
	a	(L/g)	0.2672	0.35796	0.9418
	b	$(L/mg)^n$	0.0706	0.13132	0.5148
	n	-	0.7884	0.71914	0.6477
	R^2	-	0.9987	0.9967	0.9983

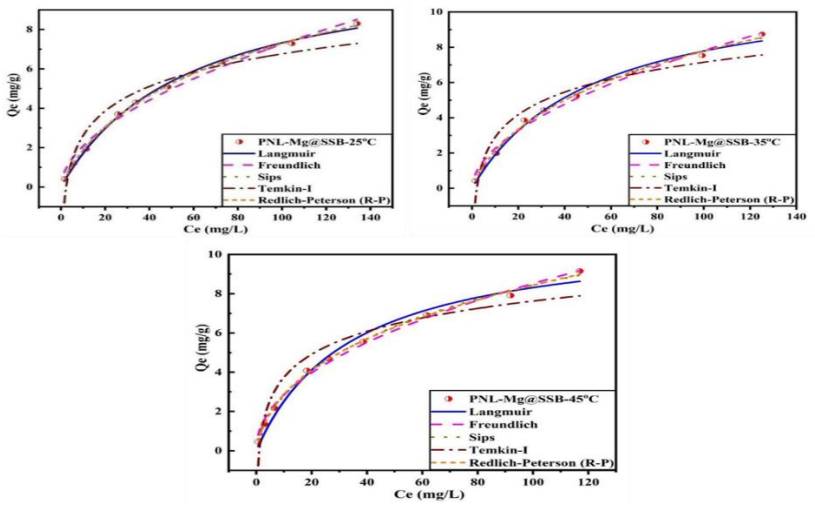

Figure 4: Isotherm fitting for PNL adsorption onto Mg-SSB at 25, 35, and 45 ºC respectively

Table 5 (b): Isotherm parameters for PCP adsorption onto Mg-SSB

Isotherm Models	Parameters	Units	25 ºC	35 ºC	45 ºC
Langmuir					
	q_{max}	(mg/g)	13.1297	13.299	12.642
	K_L	(L/mg)	0.01567	0.0214	0.0293
	R^2	-	0.9921	0.9883	0.9834
Freundlich					
	K_F	$(mg/g)(L/mg)^{-1/n}$	0.5791	0.7662	1.025
	n	-	1.7487	1.8360	2.025
	R^2	-	0.9967	0.9948	0.9972
Sips					
	q_{max}	(mg/g)	28.1647	28.9407	37.2407
	K_S	(L/g)	0.01574	0.02106	0.02424
	n	-	0.70226	0.6752	0.58468
	R^2	-	0.9984	0.9967	0.9983
Temkin-I					
	q_T	(J/mol)	1.8579	1.9945	1.7585
	K_T	(L/g)	0.4855	0.6013	1.1769
	R^2	-	0.9051	0.9223	0.9025
Redlich-Peterson (R-P)					
	a	(L/g)	0.4925	0.7338	1.7265
	b	$(L/mg)^n$	0.3591	0.4470	1.1491
	n	-	0.5777	0.5944	0.5792
	R^2	-	0.9988	0.9976	0.9988

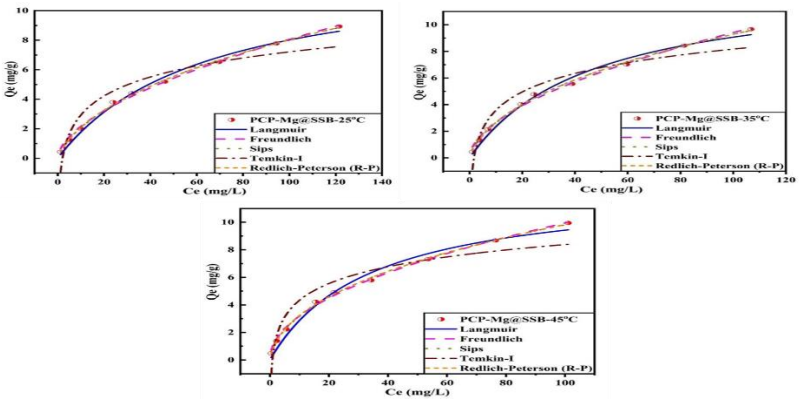

Figure 5: Isotherm fitting for PCP adsorption onto Mg-SSB at 25, 35, and 45 °C respectively

Application of Radushkevich Isotherm and its Derivatives

The use of the Radushkevich isotherm and its derivatives, including Dubinin-Radushkevich (DR), Dubinin-Astakhov (DA), and Dubinin-Radushkevich-Misra. Higher isotherms such as Temkin-II were used, and the results are compared to the Langmuir on the performance of phenol (PNL) and para-chlorophenol (PCP) on adsorption onto these modified biochar materials. Surface heterogeneity and adsorption energetics of phenol (PNL) and para-chlorophenol (PCP) were understood by interpreting the equilibrium adsorption isotherms on the surface of magnesium-modified bicarb (Mg-SSB) using different adsorption isotherm models, including Langmuir, DA, DR, DRM, and Temkin-II models. The coefficient of determination (R^2), maximum adsorption capacity (q_{max}), and calculated adsorption energy (E_a) were used as the primary parameters for assessing model suitability, while other parameters are as presented in Table 5, and the graphical fit is shown in **Figure 6**. As shown in **Table 6**, the fit ranges of DR and DA models are in the moderate range ($R^2 \approx 0.87–0.88$) with relatively low q_{max} values (≈6.5–7.3 mg g-1) and adsorption energies in the narrow range (4.03–4.38 kJ mol-1), which correspond to weak physisorption through micropore filling. The outcome signifies that the adsorption capacity of Mg-modified biochar is underestimated by the conventional Dubinin-based models. The DRM model, on the other hand, is an excellent description as the values of the R^2 coefficients are close to one (0.9986–0.9987) in both cases of the adsorbates, which indicates that the model is statistically superior. The predicted q_{max} values are remarkably high, much higher for PCP than for PNL, with a value of 57.81 mg/g for the former and 14.84 mg/g for the latter, indicating a much higher affinity of PCP towards Mg-SSB. This is confirmed by the high adsorption energies (E_a = 9.42 kJ mol-1 for PNL, 13.61 kJ mol-1 for PCP), which means that the adsorption is not of the physisorption type, but that energetically heterogeneous adsorption sites are playing an important role. The Langmuir model also demonstrates high R^2 (above 0.99) and moderate q_{max} (11.54–13.13 mg g-1), which indicates apparent monolayer adsorption; however, it does not account for the dramatic increase in adsorption capacity seen for PCP in the DRM model. Likewise, Temkin-II exhibits good fits (R^2 around 0.996-0.999) with low q_T values, which focus on the energy changes during interactions in the process of adsorption rather than the actual capacity of the adsorbent. In general, the order of the adsorbing abilities of PNL and PCP on Mg-SSB is as follows: DRM>Temkin-II≈Langmuir>DR≈DA.

Table 6: Radushkevich Isotherm Parameters for PNL/PCP Removal using Mg-SSB

Isotherm Models	Parameters	Units	PNL	PCP
DR				
	q_{max}	(mg/g)	6.94	7.32
	b	-	0.615	0.611
	E_a	(kJ/mol)	4.03	4.05
	R^2	-	0.8806	0.8781
DA				
	q_{max}	(mg/g)	6.51	6.82
	b	-	0.581	0.565
	n	-	2.00	2.00
	E_a	(kJ/mol)	4.26	4.38
	R^2	-	0.8711	0.8670
DRM				
	q_{max}	(mg/g)	14.84	57.81
	b	-	0.263	0.182
	α	-	2363	-
	E_a	(kJ/mol)	9.42	13.61
	R^2	-	0.9986	0.9987

Isotherm Models	Parameters	Units	PNL	PCP
Temkin-II				
	q_T	(mg/g)	3.53	4.13
	K_T	(L/mg)	0.0689	0.0595
	R^2	-	0.9988	0.9962
Langmuir				
	q_{max}	(mg/g)	11.54	13.13
	K_L	(L/mg)	0.0173	0.0156
	R^2	-	0.9970	0.9921

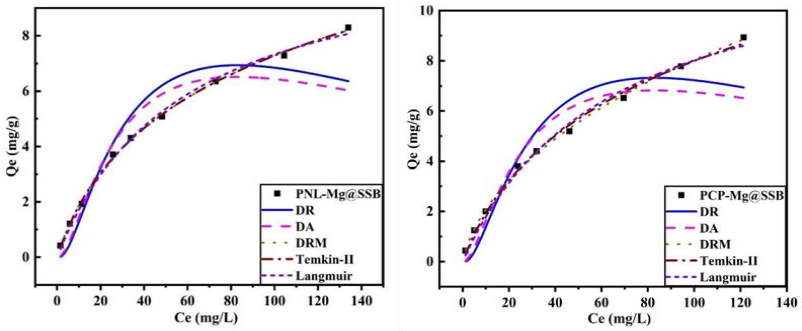

Figure 6: Radushkevich isotherm fitting for the adsorption of PNL/PCP onto Mg-SSB

Adsorption Kinetics

The adsorption kinetics of PNL and PCP onto Mg@SSB were evaluated using the pseudo-first-order (PFO), pseudo-second-order (PSO), Elovich, and Weber-Morris intraparticle diffusion (IPD) models. The PFO model provided the poorest fit, with R^2 values of 0.4448 and 0.4056 for PNL and PCP, respectively, accompanied by adjusted R^2 values of 0.3060 and 0.2571. The corresponding equilibrium adsorption capacities predicted by the model were 1.7513 and 1.8575 mg g^{-1}. These low correlation coefficients indicate that the PFO model does not adequately describe the adsorption kinetics of either phenolic compound. The PSO model showed an improved fit relative to the PFO model, giving R^2 values of 0.7109 for PNL and 0.6782 for PCP, with adjusted R^2 values of 0.6386 and 0.5977, respectively. Although these values indicate a better representation than the PFO model, the relatively low coefficients of determination demonstrate that the PSO model does not provide a strong overall description of the experimental kinetic data. The predicted equilibrium capacities were 1.8645 and 1.9878 mg g^{-1} for PNL and PCP, respectively, while the corresponding $k_2$values were 0.1312 and 0.1142 g g^{-1} min^{-1}. A considerably better correlation was obtained with the Elovich model, which produced R^2 values of 0.9067 and 0.8858 for PNL and PCP, respectively. The corresponding adjusted R^2 values were 0.8834 and 0.8573. The higher initial adsorption parameter, α, obtained for PNL (16.43 mg g^{-1} min^{-1}) compared with PCP (11.32 mg g^{-1} min^{-1}) suggests a faster initial uptake of PNL. The Elovich parameter β was 4.9963 and 4.4429 g g^{-1} for PNL and PCP, respectively, indicating a progressive decrease in the adsorption rate as the available adsorption sites became increasingly occupied. The relatively strong performance of the Elovich model is consistent with adsorption occurring on a heterogeneous surface containing sites with different adsorption energies. The Weber-Morris IPD model provided the highest correlation among the kinetic models evaluated, with R^2 values of 0.9803 for PNL and 0.9719 for PCP and adjusted R^2 values of 0.9754 and 0.9649, respectively. The corresponding intraparticle diffusion rate constants were 0.0616 and 0.0698 mg g^{-1} $min^{-1/2}$, while the intercepts were 1.1821 and 1.2149 mg g^{-1} for PNL and PCP, respectively. The non-zero intercepts indicate that the intraparticle-diffusion plots do not pass through the origin. Thus, although diffusion within the adsorbent pores contributes substantially to the overall adsorption process, intraparticle diffusion cannot be regarded as the sole rate-controlling mechanism. The intercepts further suggest a contribution from boundary-layer or external mass-transfer resistance. Hence, the kinetic results indicate that PNL and PCP adsorption onto Mg@SSB proceeds through a multistep mechanism involving surface interactions and diffusion into the porous structure rather than a single kinetic process. The superior performance of the IPD model demonstrates the important contribution of mass transport within the porous adsorbent, whereas the relatively high Elovich correlation supports the involvement of heterogeneous adsorption sites. The poor-to-moderate fits obtained from the PFO and PSO models further indicate that neither model alone adequately captures the complexity of the adsorption process.

Table 7: Kinetic models for PNL and PCP adsorption onto Mg-doped biochar

Kinetic Model	Parameter	PNL	PCP
PFO	Qe (mg/g)	1.75127	1.85754
	k_1 (min)	0.15317	0.14978
	R^2	0.44483	0.40564
	Ajd-R^2	0.30604	0.25705
PSO	Qe (mg/g)	1.86449	1.98775

Kinetic Model	Parameter	PNL	PCP
	k_2 (g/mg/min)	0.13119	0.11424
	R^2	0.71086	0.67819
	Ajd-R^2	0.63857	0.59774
Elovich	α (mg/g/min)	16.42987	11.32495
	β (g/mg)	4.99633	4.44293
	R^2	0.90672	0.88584
	Ajd-R^2	0.8834	0.8573
Weber-Moris IPD	k (mg/g/min)	0.06161	0.0698
	C (mg/g)	1.18205	1.21493
	R^2	0.9803	0.97193
	Ajd-R^2	0.97537	0.96491

Adsorption Mechanism

The interaction mechanism between pollutants and biochar materials is not a simple process; several bond formations are involved and can be studied by the analysis of the residual biochar using FT-IR techniques. The common interactions often observed in biochar remediation studies include, but are not limited to, hydrogen bond formation; n-π interaction; π-π interaction; and pore filling (Tran *et al*., 20202; Chen *et al*., 2019; Grimm *et al*., 2025). The FT-IR residual analysis (adsorbate-adsorbent interaction) shows that adsorption of PNL and PCP onto the modified SSB biochars is controlled by cooperative surface interactions, which include hydrogen bonds, n→π and π→π electron donor-acceptor interactions, depending on the type of surface modification. The pristine biochar presents surface hydroxyl (O–H) bands, characteristic bands of aromatic C=C, carbonyl C=O, and C–O functionalities, which are the main adsorption active sites in all materials. Systematic shifts, intensity changes, and band broadening are observed upon interaction with PNL & PCP, suggesting bond formation instead of physical attachment, as shown in Figure 7. In the case of Mg-SSB, the most significant changes in the spectrum are in the O–H stretching band, which is at 3323 cm^{-1}, and its shifting to 3338 cm^{-1} after adsorption of PNL and to 3359 cm^{-1} after adsorption of PCP, with clear band broadening. Both are examples of hydrogen bonding. This behaviour suggests strong hydrogen bonding interactions between the surface hydroxyl groups and the phenolic –OH of PNL and the oxygen-containing groups of PCP. Significant changes in the aromatic C=C band at 1638 cm^{-1} and changes in the C=O region at 1791 cm^{-1} suggest that the aromatic rings of the adsorbates are also undergoing more π→π stacking with the conjugated domains of the biochar. The simultaneous presence of O–H and C=C bands indicates that the Mg-SSB is capable of a mixed hydrogen-bonding/π-π interaction mechanism, which is responsible for the constant performance of its adsorption.

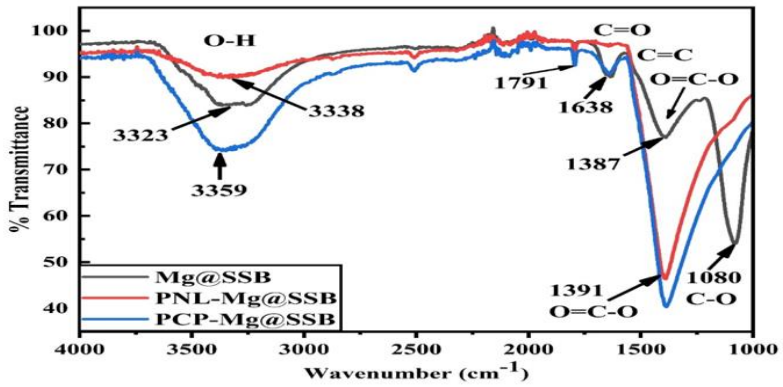

Figure 7: FT-IR residual analysis for PNL/PCP adsorption onto Mg-SSB

Theoretical Calculations

The electronic properties and adsorption capability of phenol (PNL) and p-chlorophenol (PCP) onto the magnesium-modified snail shell biochar (Mg@SSB) were studied using the Density Functional Theory (DFT) method as applied to the adsorption of water contaminants using biochar obtained from other biomass sources (Zhou *et al*., 2023; Fang *et al*., 2025). Calculations of frontier molecular orbital (FMO) parameters and adsorption energies (Eads) are discussed in Table 8. The pristine Mg@SSB surface has a HOMO energy of −4.978 eV, a LUMO energy of −2.997 eV, and a HOMO–LUMO energy gap of 1.981 eV. The small energy gap suggests high chemical activity and electronic activity of the magnesium-functionalized biochar. The calculated ionization potential (4.978 eV) and electron affinity (2.997 eV) further support the balanced electron-donating and electron-accepting properties of Mg@SSB, which are desired for adsorbents with aromatic organic pollutant interaction properties (Louis *et al*., 2026). As a result of the adsorption of chlorophenol (PCP), the HOMO energy of the composite shifts to −4.537 eV, and the LUMO energy to −2.583 eV, yielding an energy gap of 1.954 eV, which is slightly smaller than that of the pristine Mg@SSB. Accordingly, the ionization potential of the molecule drops to 4.537 eV, and its electron affinity becomes less than 2.583 eV (which indicates redistribution of electron density after adsorption). In the case of the PNL–Mg@SSB complex, the HOMO and LUMO energies were found to be −4.567 eV and −2.436 eV, respectively, which gives a value of 2.131 eV for the energy gap. The adsorption of phenol slightly widens the HOMO–

LUMO gap compared with the pristine Mg@SSB, unlike PCP. The calculated values of the ionization potential (4.567 eV) and electron affinity (2.436 eV) also suggest that the transfer of an electron is less favorable in this system than in the system of adsorption of PCP. The strength of adsorption of both pollutants is directly obtained from the adsorption energies. The adsorption energies calculated for PCP–Mg@SSB and PNL–Mg@SSB are −1.1683 eV and −0.8163 eV, respectively. The negative adsorption energies are proof that adsorption is thermodynamically spontaneous and energetically favorable for both compounds. The DFT results are also in good agreement with adsorption equilibrium studies. The adsorption capacities of PCP were found to be greater than those of phenol from the Sips, Langmuir, and DRM isotherms in the experiment. The computed HOMO–LUMO gap (1.954 eV) and adsorption energy (−1.1683 eV) values of PCP are lower, which suggests that the electronic interaction and surface binding are higher. However, the energy gap of PNL is larger (2.131 eV), and the adsorption energy is less negative (−0.8163 eV), which shows comparatively weaker adsorption. The consistency of the experimental adsorption data with the DFT calculations confirms the adsorption mechanism proposed.

Table 8: HOMO-LUMO energies, quantum descriptors, and adsorption energies of Mg@SSB and its interaction with PCP and PNL

Surfaces	**LUMO/eV**	**HOMO/eV**	**ΔE/eV**	**I/eV**	**A/eV**	**Eads**/eV
Mg-SSB	-2.997	-4.978	1.981	4.978	2.997	-
PCP-Mg-SSB	-2.583	-4.537	1.954	4.537	2.583	-1.1683
PNL-Mg-SSB	-2.436	-4.567	2.131	4.567	2.436	-0.8163

CONCLUSION

This study demonstrated that Mg modification substantially altered the physicochemical characteristics of snail-shell biochar and produced Mg@SSB with promising adsorption performance toward phenol (PNL) and para-chlorophenol (PCP). The adsorption results showed a stronger uptake tendency for PCP than PNL, which was consistently reflected in the equilibrium and computational analyses. The Dubinin-Radushkevich-Misra (DRM) model provided an excellent representation of the equilibrium data, with R^2 values of 0.9986–0.9987, exceeding those obtained from the Langmuir model. The DRM estimated maximum adsorption capacities of 14.84 mg g^{-1} for PNL and 57.81 mg g^{-1} for PCP, while the corresponding mean adsorption energies were 9.42 and 13.61 kJ mol^{-1}, respectively. These results indicate a substantially stronger adsorption affinity of Mg@SSB for PCP. The kinetic analysis further showed that adsorption was not adequately described by a single conventional kinetic model. The PFO and PSO models produced relatively low correlations, whereas the Elovich model gave considerably better fits, with R^2 values of 0.9067 and 0.8858 for PNL and PCP, respectively. The Weber-Morris model produced the highest single-model correlations ($R^2 = 0.9803$ for PNL and 0.9719 for PCP); however, its non-zero intercepts indicate that intraparticle diffusion was not the sole rate-controlling step. The DFT calculations provided molecular-level support for the experimental observations. The calculated adsorption energies for PCP–Mg@SSB and PNL–Mg@SSB were -1.1683 and -0.8163 eV, respectively, confirming the stronger interaction of PCP with the Mg@SSB surface. The electronic properties of Mg@SSB, including E_{HOMO} of −4.978 eV, E_{LUMO} of −2.997 eV, and a band gap of 1.981 eV, further indicate that the modified surface possesses electronic characteristics conducive to interaction with phenolic molecules. Overall, the combination of equilibrium modelling, kinetic analysis, experimental characterization, and DFT calculations indicate that Mg@SSB is a promising low-cost adsorbent for phenolic contaminant removal under the investigated laboratory conditions. Nevertheless, its practical application to complex wastewater requires further evaluation. In particular, regeneration and reuse, competitive adsorption in the presence of co-existing contaminants, adsorbent stability, continuous-flow/column performance, and treatment of real wastewater should be investigated before scale-up and field application.

REFERENCES

Ahmaruzzaman, M., Mishra, S. R., Gadore, V., Yadav, G., Roy, S., Bhattacharjee, B., ... & Kumari, K. (2024). Phenolic compounds in water: from toxicity and source to sustainable solutions-an integrated review of removal methods, advanced technologies, cost analysis, and prospects. *Journal of Environmental Chemical Engineering*, 112964. https://doi.org/10.1016/j.jece.2024.112964

Alumonah, J. A., Emeke, C., Ehihamen, P. E., Igwegbe, C. A., & Onyechi, K. (2024, August). Snail shells as sustainable remediation agents: A novel approach to removing heavy metals from produced water in the oil and gas industry. In *SPE Nigeria Annual International Conference and Exhibition* (p. D021S004R002). SPE.

An, J., Nhung, N. T. H., Ding, Y., Chen, H., He, C., Wang, X., & Fujita, T. (2022). Chestnut shell-activated carbon mixed with pyrolytic snail shells for methylene blue adsorption. *Materials*, *15*(22), 8227. https://doi.org/10.3390/ma15228227

Chen, S., Qin, C., Wang, T., Chen, F., Li, X., Hou, H., & Zhou, M. (2019). Study on the adsorption of dyestuffs with different properties by sludge-rice husk biochar: adsorption capacity, isotherm, kinetic, thermodynamics and mechanism. *Journal of Molecular Liquids*, *285*, 62-74. https://doi.org/10.1016/j.molliq.2019.04.035

Chu, K. H. (2021). Revisiting the Temkin isotherm: dimensional inconsistency and approximate forms. *Industrial & Engineering Chemistry Research*, *60*(35), 13140-13147. https://pubs.acs.org/doi/abs/10.1021/acs.iecr.1c01788

Chu, K. H., Debord, J., Harel, M., & Bollinger, J. C. (2022). Mirror, mirror on the wall, which is the fairest of them all? Comparing the Hill, Sips, Koble–Corrigan, and Liu adsorption isotherms. *Industrial & Engineering Chemistry Research*, *61*(19), 6781-6790. https://pubs.acs.org/doi/abs/10.1021/acs.iecr.2c00507

Chu, K. H., Hashim, M. A., da Costa Santos, Y. T., Debord, J., Harel, M., & Bollinger, J. C. (2024). The Redlich–Peterson isotherm for aqueous phase adsorption: Pitfalls in data analysis and interpretation. *Chemical Engineering*

Science, *285*, 119573. https://doi.org/10.1016/j.ces.2023.119573

Chu, K. H., Hashim, M. A., Hayder, G., & Bollinger, J. C. (2024). Comparative evaluation of the Dubinin–Radushkevich isotherm and its variants. *Industrial & Engineering Chemistry Research*, *63*(34), 15002-15011. https://pubs.acs.org/doi/abs/10.1021/acs.iecr.4c01895

Dennington, R., Keith, T. A., & Millam, J. M. (2016). *GaussView, Version 6*. Semichem Inc., Shawnee Mission, KS.Dong, F. X., Yan, L., Zhou, X. H., Huang, S. T., Liang, J. Y., Zhang, W. X., ... & Diao, Z. H. (2021). Simultaneous adsorption of Cr (VI) and phenol by biochar-based iron oxide composites in water: Performance, kinetics and mechanism. *Journal of Hazardous Materials*, *416*, 125930. https://doi.org/10.1016/j.jhazmat.2021.125930

Fang, Y., Tang, Y., Li, G., Dong, J., Ye, C., Bu, Z., & Guo, W. (2025). Synergistic adsorption mechanisms of self-N-doped biochar for levofloxacin elimination: integrated experimental and DFT studies. *Environmental Research*, 122634. https://doi.org/10.1016/j.envres.2025.122634

Frisch, M. J., Trucks, G. W., Schlegel, H. B., Scuseria, G. E., Robb, M. A., Cheeseman, J. R., Scalmani, G., Barone, V., Petersson, G. A., Nakatsuji, H., Li, X., Caricato, M., Marenich, A. V., Bloino, J., Janesko, B. G., Gomperts, R., Mennucci, B., Hratchian, H. P., Ortiz, J. V., ... Fox, D. J. (2016). *Gaussian 16 Revision C.01*. Gaussian Inc., Wallingford, CT.Fseha, Y. H., Shaheen, J., & Sizirici, B. (2023). Phenol contaminated municipal wastewater treatment using date palm frond biochar: Optimization using response surface methodology. *Emerging Contaminants*, *9*(1), 100202. https://doi.org/10.1016/j.emcon.2022.100202

Gómez-Pastora, J., Bringas, E., & Ortiz, I. (2014). Recent progress and future challenges on the use of high-performance magnetic nano-adsorbents in environmental applications. *Chemical Engineering Journal*, *256*, 187-204. https://doi.org/10.1016/j.cej.2014.06.119

Grimm, A., Conrad, S., Gentili, F. G., Mikkola, J. P., Hu, T., Lassi, U., ... & dos Reis, G. S. (2025). Highly efficient boron/sulfur-modified activated biochar for removal of reactive dyes from water: Kinetics, isotherms, thermodynamics, and regeneration studies. *Colloids and Surfaces A: Physicochemical and Engineering Aspects*, *713*, 136486. https://doi.org/10.1016/j.colsurfa.2025.136486

Grimme, S., Antony, J., Ehrlich, S., & Krieg, H. (2010). A consistent and accurate ab initio parametrization of density functional dispersion correction (DFT-D) for the 94 elements H–Pu. *The Journal of Chemical Physics*, *132*(15), 154104. https://doi.org/10.1063/1.3382344

Guo, Z., Zhang, D., Ma, L., Dai, Q., Yang, R., & Ao, R. (2025). Magnesium-modified algae biochar for phosphorus adsorption: Synthesis, experimental analysis, DFT calculations, and regeneration. *Journal of Water Process Engineering*, *71*, 107169. https://doi.org/10.1016/j.jwpe.2025.107169

Hamdaoui, O., & Naffrechoux, E. (2007). Modeling of adsorption isotherms of phenol and chlorophenols onto granular activated carbon: Part I. Two-parameter models and equations allowing determination of thermodynamic parameters. *Journal of Hazardous Materials*, *147*(1-2), 381-394. https://doi.org/10.1016/j.jhazmat.2007.01.021

Hassan, M., Liu, Y., Naidu, R., Parikh, S. J., Du, J., Qi, F., & Willett, I. R. (2020). Influences of feedstock sources and pyrolysis temperature on the properties of biochar and functionality as adsorbents: A meta-analysis. *Science of the Total Environment*, *744*, 140714. https://doi.org/10.1016/j.scitotenv.2020.140714

Ji, X., Liu, Y., Gao, Z., Lin, H., Xu, X., Zhang, Y., ... & Duan, J. (2024). Efficiency and mechanism of adsorption for imidacloprid removal from water by Fe-Mg co-modified water hyacinth-based biochar: Batch adsorption, fixed-bed adsorption, and DFT calculation. *Separation and Purification Technology*, *330*, 125235. https://doi.org/10.1016/j.seppur.2023.125235

Karami, A., Sabouni, R., & Ghommem, M. (2020). Experimental investigation of competitive co-adsorption of naproxen and diclofenac from water by an aluminum-based metal-organic framework. *Journal of Molecular Liquids*, *305*, 112808. https://doi.org/10.1016/j.molliq.2020.112808

Kujawski, W., Warszawski, A., Ratajczak, W., Porębski, T., Capała, W., & Ostrowska, I. (2004). Application of pervaporation and adsorption to the phenol removal from wastewater. *Separation and Purification Technology*, *40*(2), 123-132. https://doi.org/10.1016/j.seppur.2004.01.013

Kumar, N. S., Shaikh, H. M., Asif, M., & Al-Ghurabi, E. H. (2021). Engineered biochar from wood apple shell waste for high-efficient removal of toxic phenolic compounds in wastewater. Scientific Reports, 11(1), 2586. https://doi.org/10.1038/s41598-021-82277-2

Lima, E. C., Sher, F., Guleria, A., Saeb, M. R., Anastopoulos, I., Tran, H. N., & Hosseini-Bandegharaei, A. (2021). Is one performing the treatment of adsorption kinetics data correctly?. *Journal of Environmental Chemical Engineering*, *9*(2), 104813. https://doi.org/10.1016/j.jece.2020.104813

Louis, H., Egbuchunam, T. O., Orisakwe, V. K., & Mbonu, I. J. (2026). Synthesis and Computational Evaluation of PET-based Polymer Composites for the Adsorption of Chlorophenol. *UMYU Scientifica*, *5*(2), 241-255.

Mahanty, B., Behera, S. K., & Sahoo, N. K. (2023). Misinterpretation of Dubinin–Radushkevich isotherm and its implications on adsorption parameter estimates. *Separation Science and Technology*, *58*(7), 1275-1282. https://doi.org/10.1080/01496395.2023.2189050

Mhlongo, L. N. (2021). *Ecological and human health risk assessment of selected endocrine disrupting phenolic compounds in potable water and treated wastewater effluent in the Western Cape, South Africa* (Doctoral dissertation, Cape Peninsula University of Technology).

Mikolajczyk, A. P., Holmes, A., Berry, J. C., Gang, D. D., Hernandez, R., Holmes, W. E., & Zappi, M. E. (2026). Removal of 2, 4-Dichlorophenol Using Sustainable, Natural Adsorbents Derived from Biomass Sources: A Comparative Study of Adsorption Performance. *ACS Sustainable Resource*

Management. https://pubs.acs.org/doi/abs/10.1021/acssusresmgt.6c00047

Mustapha, S. I., Muritala, K. B., Afolabi, A. M., Alhaji, M. H., Adewoye, T. L., & Aderibigbe, F. A. (2026). Phenol removal from pharmaceutical effluent using silver doped magnetite biochar: adsorption efficiency and kinetic studies. *Chemical Engineering Communications*, *213*(1), 21-41. https://doi.org/10.1080/00986445.2025.2519294

Nhung, N. T. H., Long, V. D., & Fujita, T. (2023). A Critical Review of Snail Shell Material Modification for Applications in Wastewater Treatment. *Materials*, *16*(3), 1095. https://doi.org/10.3390/ma16031095

Panigrahy, N., Priyadarshini, A., Sahoo, M. M., Verma, A. K., Daverey, A., & Sahoo, N. K. (2022). A comprehensive review on ecotoxicity and biodegradation of phenolics: Recent progress and future outlook. *Environmental Technology & Innovation*, *27*, 102423. https://doi.org/10.1016/j.eti.2022.102423

Qiu, B., Shao, Q., Shi, J., Yang, C., & Chu, H. (2022). Application of biochar for the adsorption of organic pollutants from wastewater: Modification strategies, mechanisms and challenges. *Separation and Purification Technology*, *300*, 121925. https://doi.org/10.1016/j.seppur.2022.121925

Rai, R. K., Serra-Maia, R., Shi, Y., Psarras, P., Vojvodic, A., & Stach, E. A. (2025). Enhanced mineral carbonation on surface-functionalized MgO as a proxy for mine tailings. *Environmental Science: Nano* https://doi.org/10.1039/d4en00940a

Saghir, S., Pu, C., Fu, E., Wang, Y., & Xiao, Z. (2022). Synthesis of high surface area porous biochar obtained from pistachio shells for the efficient adsorption of organic dyes from polluted water. *Surfaces and Interfaces*, *34*, 102357. https://doi.org/10.1016/j.surfin.2022.102357

Schmidt, H. P., Bucheli, T., Kammann, C., Glaser, B., Abiven, S., & Leifeld, J. (2016). European biochar certificate-guidelines for a sustainable production of biochar.

Tomczyk, A., Sokołowska, Z., & Boguta, P. (2020). Biochar physicochemical properties: pyrolysis temperature and feedstock kind effects. *Reviews in Environmental Science and Bio/Technology*, *19*(1), 191-215. https://doi.org/10.1007/s11157-020-09523-3

Tran, H. N., Tomul, F., Ha, N. T. H., Nguyen, D. T., Lima, E. C., Le, G. T., ... & Woo, S. H.(2020). Innovative spherical biochar for pharmaceutical removal from water: Insight into adsorption mechanism. *Journal of Hazardous Materials*, *394*, 122255. https://doi.org/10.1016/j.jhazmat.2020.122255

Vu, M. T., Hoang, L. T. T. T., & Dao, M. T. (2024). Pyrolysis of Golden Snail Shells (Pomacea canaliculata L.) for Phosphorus Removal from Aqueous Solutions. *Chemical and Biochemical Engineering Quarterly*, *38*(4), 301-311. https://doi.org/10.15255/CABEQ.2024.2323

Wang, W., Xiong, P., Zhang, H., Zhu, Q., Liao, C., & Jiang, G. (2021). Analysis, occurrence, toxicity and environmental health risks of synthetic phenolic antioxidants: A review. *Environmental Research*, *201*, 111531. https://doi.org/10.1016/j.envres.2021.111531

Weigend, F., & Ahlrichs, R. (2005). Balanced basis sets of split valence, triple zeta valence and quadruple zeta valence quality for H to Rn: Design and assessment of accuracy. *Physical Chemistry Chemical Physics*, *7*(18), 3297–3305. https://doi.org/10.1039/B508541A

Yang, C. H. (1998). Statistical mechanical study on the Freundlich isotherm equation. *Journal of colloid and interface science*, *208*(2), 379-387. https://doi.org/10.1006/jcis.1998.5843

Yang, X., Jiang, D., Cheng, X., Yuan, C., Wang, S., He, Z., & Esakkimuthu, S. (2022). Adsorption properties of seaweed-based biochar with the greenhouse gases (CO_2, CH_4, N_2O) through density functional theory (DFT). *Biomass and Bioenergy*, *163*, 106519. https://doi.org/10.1016/j.biombioe.2022.106519

Yin, Y., Wang, G., Li, Q., Zhao, Z., Guo, Z., Zhang, F., ... & Liu, C. (2025). Optimizing biochar structure via two-step pyrolysis for uniform magnesium oxide post-doping with enhanced phosphate removal performance. *Colloids and Surfaces A: Physicochemical and Engineering Aspects*, *724*, 137438. https://doi.org/10.1016/j.colsurfa.2025.137438

Yu, H., Zhang, Y., Wang, L., Tuo, Y., Yan, S., Ma, J., ... & Han, L. (2024). Experimental and DFT insights into the adsorption mechanism of methylene blue by alkali-modified corn straw biochar. *RSC advances*, *14*(3), 1854-1865. https://doi.org/10.1039/d3ra05964b

Yu, Q., Feng, J., Li, J., He, A., & Sheng, G. D. (2021). Mechanisms of aromatic molecule- Oxygen-containing functional group interactions on carbonaceous material surfaces. *Chemosphere*, 275, 130021. https://doi.org/10.1016/j.chemosphere.2021.130021

Zhou, P., Li, X., Zhou, J., Peng, Z., Shen, L., & Li, W. (2023). Insights of the adsorption mechanism of methylene blue on biochar from phytoextraction residues of Citrus aurantium L.: Adsorption model and DFT calculations. *Journal of Environmental Chemical Engineering*, *11*(5), 110496. https://doi.org/10.1016/j.jece.2023.110496